Environmental Earth Sciences (2024) 83:9
https://doi.org/10.1007/s12665-023-11325-z

ORIGINAL ARTICLE

Experimental timing of pyrite oxidation under various leaching conditions: consequences for rates of weathering in geological profiles

Julien Poot[1] · Alexandre Felten[2] · Julien L. Colaux[2] · Rachel Gouttebaron[2] · Guillaume Lepêcheur[1,3] · Gaëtan Rochez[1] · Johan Yans[1]

Received: 7 July 2023 / Accepted: 22 November 2023 / Published online: 16 December 2023

Abstract
Pyrite (FeS_2) is one of the most abundant sulfides on Earth and has already been studied in numerous ways for decades because of its rapid oxidation and the associated environmental impacts. This study proposes a new experimental physico-chemical approach (air, tridistilled water and water drip exposure) to determine the oxidation rate of pyrite using surface and depth data via XPS (X-ray Photoelectron Spectroscopy) analyses. Our experimental study of almost pure pyrite reveals a maximum oxidation rate of 11.7 ± 1.8 nm day^{-1} for drip exposure with precipitation of sulfates or Fe-oxides depending on the experimental condition. The oxidation rates obtained under various experimental conditions may be extrapolated to weathering rates of different zones of supergene profiles/ores (leached zone, saprolite and cementation zone). The extrapolation suggests a maximum rate of 4.3 ± 0.6 m Ma^{-1}, which is consistent with data obtained by isotope dating of weathering profiles. Under geological conditions however, the oxidation rate of pyrite may be influenced by additional parameters, such as the nature of the host rock, its porosity/permeability, the climate, the influence of an oxidizing environment, and the mineralization of secondary minerals.

Keywords Pyrite · Oxidation rate · Weathering · XPS

Introduction

Mining and mineral processing are critical components of metal producing industries. These have grown considerably over the last few decades, thanks to advancing technologies that require more specific metals. Consequently, they generate huge amounts of waste that can lead to acid mine drainage (AMD) all over the world (Kefeni et al. 2017; Park et al. 2019; Nyström et al. 2021). During AMD, metals are typically released through leaching of sulfides (mostly pyrite), by meteoric water, which oxidize and release sulfuric acid. In addition to the acidity, the leached fluids frequently contain trace elements that can be toxic to ecosystems and/or humans (Nyström et al. 2021). Pyrite oxidation can be described by several chemical reactions depending on the oxidation conditions (Eqs. 1 and 2), in humid air (Eq. 3) and under anaerobic conditions (Eq. 4) (Garrels and Thompson 1960; McKibben and Barnes 1986; Jerz and Rimstidt 2004; Neculita et al. 2007). The release of Fe^{2+} ions can also lead to formation of Fe^{3+}, which also increases the acidity (Eq. 5) (Nordstrom 1982). The role of bacteria in the AMD process with formation of thiosulfate is illustrated in Eqs. 6 and 7 (Melashvili et al. 2015):

$$FeS_{2_{(s)}} + {}^{7}/_{2}O_{2_{(aq)}} + H_2O \rightarrow Fe^{2+} + 2SO_4^{2-} + 2H^+ \quad (1)$$

$$FeS_{2_{(s)}} + {}^{15}/_{4}O_{2_{(aq)}} + {}^{7}/_{2}H_2O \rightarrow Fe(OH)_{3_{(s)}} + 2SO_4^{2-} + 4H^+ \quad (2)$$

$$FeS_{2_{(s)}} + {}^{7}/_{2}O_2 + H_2O \rightarrow Fe^{2+} + 2SO_4^{2-} + 2H^+ \quad (3)$$

✉ Julien Poot
julien.poot@unamur.be

[1] Department of Geology, Institute of Life-Earth-Environment (ILEE), University of Namur, Rue de Bruxelles 61, 5000 Namur, Belgium

[2] Department of Physics, Namur Institute of Structured Matter (NISM), Synthesis, Irradiation and Analysis of Materials (SIAM), University of Namur, Rue de Bruxelles 61, 5000 Namur, Belgium

[3] Division of Geology, Department Earth and Environmental Sciences, KU Leuven, Celestijnenlaan 200E, 3001 Leuven, Belgium

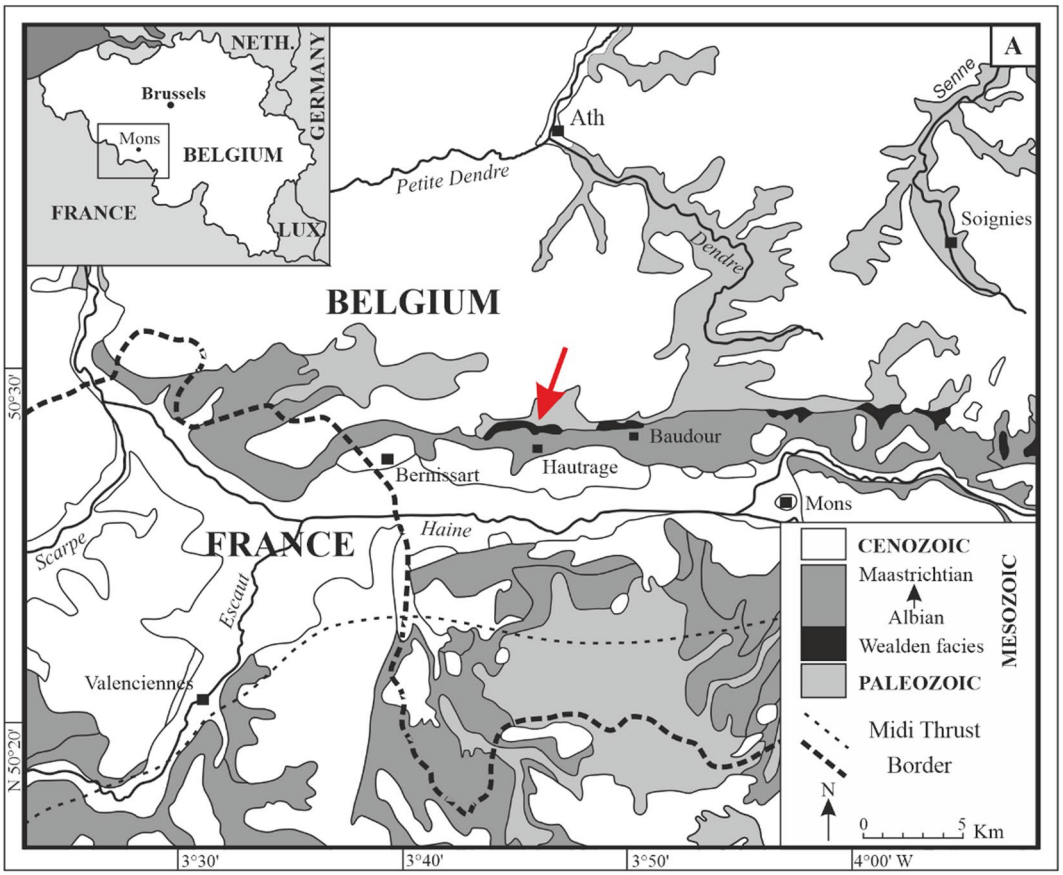
A
NETH.
Brussels
Mons
BELGIUM
GERMANY
FRANCE
LUX
Ath
Petite Dendre
Senne
Dendre
Soignies
BELGIUM
Baudour
Bernissart
Hautrage
Mons
FRANCE
Haine
Scarpe
Escaut
Valenciennes
CENOZOIC
Maastrichtian
Albian
Wealden facies
PALEOZOIC
MESOZOIC
Midi Thrust
Border
N
0
5 Km
50°30'
N 50°20'
3°30'
3°40'
3°50'
4°00' W


C


D

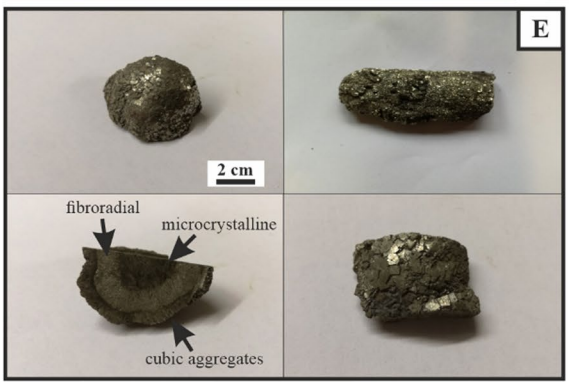
E
2 cm
fibroradial
microcrystalline
cubic aggregates

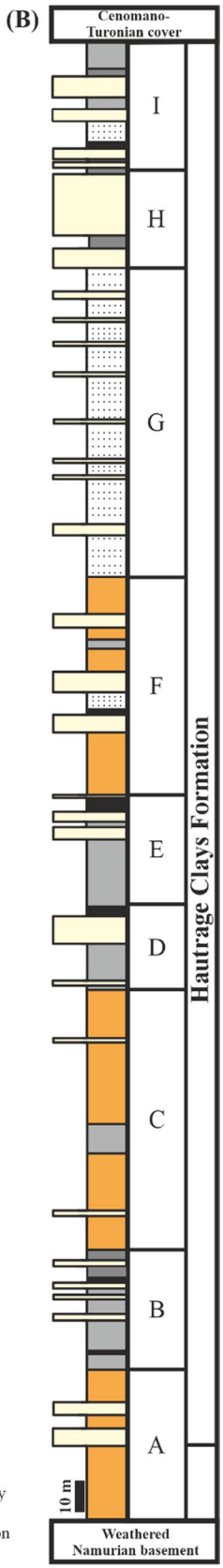
(B)
Cenomano-
Turonian cover
I
H
G
F
E
D
C
B
A
Hautrage Clays Formation
10 m
Weathered
Namurian basement
Sand
Massive clay
Roots and pseudo-mycellium clay
Clay with siderite nodules
Accumulation of debris vegetation
Finely laminated clay

◂**Fig. 1** **A** Simplified geological map of Mons Basin. Location of Hautrage and Wealden facies sediments (in black) on the northern border of the Basin (modified from Yans et al. 2005). **B** Simplified lithological log of the Hautrage Clay Formation deposits (Spagna et al. 2011). **C** General view of the Hautrage quarry showing the black level (unit G). **D** Black clay level for pyrite sampling. **E** Nodular and wood-related pyrite sampled from black clays (unit G)

$$FeS_{2(s)} + 14Fe^{3+} + 8H_2O \rightarrow 15Fe^{2+} + 2SO_4^{2-} + 16H^+ \quad (4)$$

$$Fe^{2+} + {}^1/_4O_2 + {}^5/_2H_2O \rightarrow Fe(OH)_3 + 2H^+ \quad (5)$$

$$2FeS_2 + H_2O + 1.5O_2 \rightarrow 2FeOOH + 4S^0 \quad (6)$$

$$4S^0 + 4OH^- \rightarrow 2HS^- + S_2O_3^{2-} + H_2O \quad (7)$$

The oxidation of pyrite has already been modeled extensively, providing various oxidation rates (McKibben and Barnes 1986; Nicholson et al. 1990; Williamson and Rimstidt 1994; Jerz and Rimstidt 2004; Lapakko and Antonson 2006). These models are mainly based on the specific surface area of pyrite: the surface reaction rate is calculated as the amount of change in reactants or products divided by the total surface area of pyrite. Here, we performed new experiments on the evolution of pyrite at depth under various conditions using XPS (X-ray photoelectron spectroscopy) in order to propose an analogy with the evolution of weathering profiles. This study deals with almost pure pyrites that are similar to the synthetic pyrites sometimes used for the mentioned models; our studied samples remain natural to simulate natural conditions. Our experimental results will be extrapolated to describe the evolution of pyrite in geological weathering profiles, their rate depending on several factors discussed in this article. The formation rate of these weathering profiles, which can be of economic interest, has already been estimated by isotope dating methods (e.g., Vasconcelos and Conroy 2003; Braun et al. 2012; De Putter et al. 2015), which will be compared to those provided experimentally in this study.

Geological settings

Geology of Mons Basin

Pyrite samples were collected in the Danube–Bouchon quarry (Hautrage, Belgium), in the mining Wealden facies sediments of the Mons Basin (Fig. 1A). The Mons Basin is a geological unit almost 40 km long and 10 km wide on the NE edge of the Anglo–Paris basin. Its formation is the result of a combination of deep karstic and tectonic subsidence caused by the partial dissolution of thick levels of anhydrites and the reactivation of ante-Cretaceous faults at an extensive regional context (Dupuis and Vandycke 1989; Vandycke et al. 1991; Spagna et al. 2011). The rocks of the Mons Basin consist of Meso–Cenozoic sediments, all unconformably deposited on the Paleozoic basement that has been folded and faulted during the Variscan orogeny (Marlière 1954). In the Mons Basin, the Wealden facies sediments are the products of continental erosion ranging from middle Barremian to late Albian (Schnyder et al. 2009; Yans et al. 2010).

Danube–Bouchon quarry

The Danube–Bouchon quarry (city of Hautrage) exploits the Wealden facies sediments of the Hautrage Clay Formation (HCF), which are mainly used for the manufacture of refractory materials and concrete. The HCF forms layers and lenses of a thickness of a few decimeters to several meters, with grain sizes ranging from clay to sand, hosting many plant fossils (Barral et al. 2016, 2017). The deposit is stratified with a direction from N95° E to N105° E, and a dip of 10°–25° (Yans 2007). These sediments are interpreted as a fluviatile environment (Spagna et al. 2012).

The HCF (~ 230 m thick) is divided into 9 different zones from bottom to top (Fig. 1B) (Spagna et al. 2011, 2012): (i) approximately 85 m of reddish clay facies with siderite ($FeCO_3$) nodules (units A to C); (ii) white, greyish, blueish, brownish or black clays intersected by lenses of sand and levels of pyritized plant debris of a total thickness of 112 m (units D to G); (iii) 35 m of sandy, sometimes conglomeratic sediments with some clayey intercalations that are rich in plant debris (units H and I). Only the upper units (E to I) are still visible in the Danube–Bouchon quarry (Yans 2007). The mineralogy of clays of HCF is mainly characterized by illite, kaolinite, chlorite and various mixed-layers minerals (Yans et al. 2010). A black clay level (Fig. 1C, D), rich in wood debris and pyrite, is observed in the upper zone of unit G (Fig. 1E). Yans (2007) suggests that the formation of pyrite in HCF is related to organic debris being epigenized into pyrite during early diagenesis.

Materials and methods

Sampling, experimental oxidation and chemical analyses

Pyrite samples (Fig. 1E) were collected from the black clay level of the upper zone of Unit G (HCF). The collected pyrites were washed with tridistilled water directly after sampling to remove residual clays. A representative number of pyrites were analyzed by XPS to ensure that

they were unoxidized/fresh before starting the experimental oxidation. The pyrite nodules show cubic aggregates on the surface, followed by a fibroradial "crown" and a microcrystalline pyrite in its center (Fig. 1E). Only the outer cubic crystals were used for the experiment here. Pyrites associated with wood were not used because of slight or even intense oxidation (= not "fresh").

After sampling and cleaning, each pyrite was numbered and exposed to various experimental conditions: (i) air (20 samples); (ii) tridistilled water (15 samples); (iii) or exposure to a continuous water drip simulating a flow (25 samples). The lab conditions were as follows: atmospheric pressure (1 bar), humidity between 45 and 55%, temperature between 19 and 23 degrees Celsius. Tridistilled water (Milli-Q) has a low conductivity (5.4 µS/cm) and pH ~ 5.8 (mostly dissolved CO_2), which is similar to rainwater pH but lacking solubilized elements.

For the drip exposure we used an ISMATEC© Perstaltic Ecoline VC MS/CA 8/6 pump with 8 tubes of Ismaprene (0.51 mm diameter) connected to a tridistilled water tank of 50 L (ESM1). Each tube simulates a non-permanent flow (0.1 ml/min) over the pyrite. For each type of experiment (air, water, drip exposure), oxidation is analyzed at different points in time, from $t = 0$ to 10,000 h. To stop the oxidation process at a given time, the samples are removed from the exposure system and placed in a vacuum chamber at a pressure of 10^{-7} mbar, waiting for XPS measurements. For each sample, at least one surface and one depth measurement were performed on a planar/smooth surface (cubic grains).

Chemical analyses were carried out by Activation Laboratories Ltd. (Actlabs, Canada). Major elements were identified with the help of FUS–ICP (Fusion Inductively Coupled Plasma Optical Emission Spectrometry) while the reduced iron (FeO) was determined by titration. Trace elements were analyzed by FUS–MS (Mass Spectrometry) while S was measured using the IR method (Infrared).

XPS surface and depth-profile analyses

XPS measurements were performed using a K-alpha spectrometer (Thermofisher), equipped with a monochromatic Al Kα source (1,486.6 eV) with a spot size of 300 µm. The Thermo Avantage software was used for data processing. Survey and high-resolution spectra were calibrated with C_{1s} with an energy step of 1.0 and 0.1 eV, and a pass energy of 200 eV and 20 eV respectively. Spectra recorded during the depth profiles were measured using the so-called snapshot mode. This mode allows to acquire faster profiles with sufficient energy resolution to separate sulfate and sulfide peaks. The sputtering was performed using Ar^+ ions with an energy of 2 keV and a raster size of 1.5×1.5 mm^2. A flood gun with combined electron and low energy ions was also used during analysis to prevent surface charging. The depth profile analysis consists of several sputtering steps ranging from 5 to 30 s, depending on the total profile time to be reached. After each sputtering step, measurements of S 2*p*, Fe $2p_{3/2}$, O 1s, Si_{2p} and C_{1s} were performed using a snapshot acquisition. For S 2*p* and Fe 2*p*3/2 spectra, the different peaks and binding energies associated with pyrite and oxidation products are listed in Table 1. Ar^+ sputtering can slightly affect the structure of the pyrite to form some Fe–S-type surface species resulting in a small flat peak at 708.8 eV (Karthe et al. 1993), which is, however, negligible compared to the induced oxidation processes and which can be easily discerned from the oxidized species formed (sulfates and Fe-oxides).

The sputtering rate was evaluated by measuring the depth of the crater that was left after the sputtering process on polished pyrite, using a DektakXT stylus profilometer by Bruker© (Fig. 2A). The average sputtering rate was 0.6 nm. s^{-1} and is reproducible. The applied XPS measurements provide exact information on the elemental composition of samples with an excellent depth resolution (< 10 nm). Despite the oxidation process being relatively slow, this method allows to determine the evolution of the oxidation

Table 1 XPS binding energies for relevant chemical species

Species	Binding energy (eV)	References	Species	Binding energy (eV)	References
Fe $2p_{3/2}$			S 2*p*		
Fe(II)–S	707.4	Karthe et al. (1993)	S^{2-}	161.1	Buckley and Woods (1987)
(Pyrite)	707.1	Eggleston et al. (1996)		161.3	Pratt et al. (1994)
FeO	709.6	Mills and Sullivan (1983)	S_2^{2-}	162.5	van der Heide et al. (1980)
Fe_3O_4	710.8	Mills and Sullivan (1983)		162.4	Eggleston et al. (1996)
α-Fe_2O_3	711.0	Harvey and Linton (1981)	S_8	163.7	Hyland and Bancroft (1990)
α-FeOOH	711.9	Ferris et al. (1989)		163.8	Wanger et al. (1979)
	712.1	Scheidegger et al. (1993)	SO_4^{2-}	169.1	Wanger et al. (1979)
				168.5	(Jones et al. (1992)

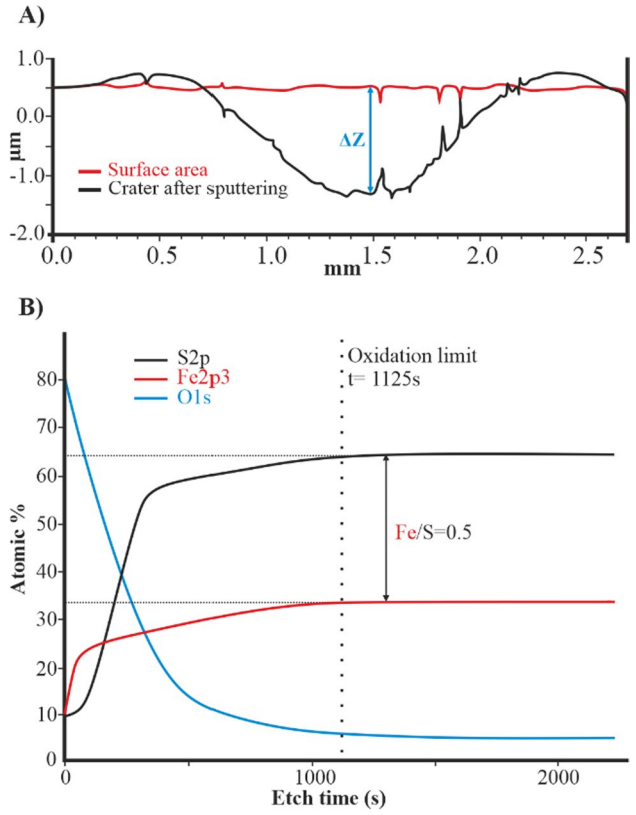

Fig. 2 **A** Example of a DektakXT profile and crater depth measurement (ΔZ) for 3000 s sputtering. (**B**) Determination of the oxidation limit with Fe/S ratio and oxygen from XPS profile on pyrite

depth already within a single year in the laboratory, while the natural process takes place over thousands or even millions of years. Moreover, the data on chemical bonds allow to distinguish pyrite (Fe-sulfides) from Fe-sulfates or even Fe-oxides, even if they occur only in small quantities and in depth. However, the shortcoming of this method is its limited sensitivity (~0.1 at. %). Therefore, XPS cannot determine the evolution of trace elements, which were monitored by FUS–MS and hardly impacted the experiments.

For each depth profile, the thickness of the oxidation layer was derived from several characteristics: the Fe/S ratio, the oxygen concentration of the depth profile, and the presence of sulfates or oxides (mostly iron). The evolution of S, Fe and O concentrations of a typical XPS depth profile is shown in Fig. 2B. The oxygen content is never zero due to the shadowing effect and roughness of the sample, but it remains stable when no more oxidation happens (which is also observed for fresh pyrite). The limit of the oxidized layer is also characterized by a Fe/S ratio of 0.5 (Fig. 2B, etching time 1125 s). It should be noted that a Si signal can reveal the presence of a potential clay-filled (micro)fracture, which would affect the result. Once the limits of the oxidation layer are defined, the associated sputtering time is converted to oxidation depth by using the sputtering rate. Error bars are mainly caused by slight variabilities in depth profile measurements, but also by the natural character of pyrite causing variation in experimental time periods. Thus, for a given time period, the error bar represents both the variability of the oxidation depth between samples, and the measurement error of the crater depth with DektakXT, which is, however, negligible compared to the natural variability of the sample.

Results

Chemical analyses of the outer part of the pyrite nodules (Fig. 1E; "crown" used for the XPS analyses) performed with FUS–ICP/MS are listed in Table 2. The pyrite was composed of 52.5 wt.% S and 45.3 wt.% Fe which corresponds to a 2.018 S/Fe molar ratio. Other elements were poorly represented except for SiO_2 (0.61 wt.%) and Al_2O_3 (0.13 wt.%). The concentration of Ni, Ba, Mo, Cr, Zn, As and Cu (main trace elements) was 80, 28, 27, 20, 20, 14 and 10 wt.ppm, respectively.

The oxidation depth results obtained by XPS for the different experiments (air, water and drip exposure) are shown in Fig. 3.

For pyrite in tridistilled water (Fig. 3A, B), initial oxidation was fast but saturated at a shallow depth: 150–200 nm at 2000 h ($y = 0.0714x$, $R^2 = 0.88$). Following this rapid evolution, the oxidation continued to slightly increase up to 10,000 h with a very gentle slope ($y = 0.000690x + 162$, $R^2 = 0.82$), corresponding to an oxidation rate of 0.017 nm. day^{-1}. On the samples for the 10,000 h experiment, no sulfate or oxide could be noticed macroscopically (Fig. 3C) or by XPS: pyrite exposed to tridistilled water was macroscopically comparable to fresh pyrite (Fig. 1E). The progression of the pH-value of the water was also measured (Fig. 4) until 2,500 h, distinguishing between "pure" pyrite and pyrite containing low residual clay fractions from the HCF. The initial pH (5.8) equaled the pH of the tridistilled water. For "pure" pyrite the pH dropped rapidly to 3.5–4, then decreased less significantly and stabilized at around 2.2–2.5 after 2,000 h. The pH values were again measured at 5,000 h and 10,000 h and varied between 2.2–2.4 and 2.1–2.3, respectively, depending on the sample. This evolution of the pH suggests that oxidation of the pyrite was slightly ongoing, which has been confirmed by XPS observations (Fig. 3A), but macroscopically undetectable.

For air exposure (Fig. 3A), initial oxidation depth increased rapidly during the first 2,000 h (~80 days) with a slope of 0.174 nm h^{-1} ($R^2 = 0.97$) to reach about 320 nm. Afterwards, the oxidation process was much slower with a slope of 0.0115 nm h^{-1} ($R^2 = 0.75$). For this second trend, data are more scattered and vary more significantly depending on the pyrite sample, resulting in larger error bars. For

Table 2 Major (wt. %) and trace elements (wt.ppm) in pyrite from the Danube–Bouchon (Hautrage) quarry

Major	S(tot) 52.5	FeO 45.3	SiO_2 0.61	Al_2O_3 0.13	MnO 0.011	MgO 0.02	CaO 0.08	Na_2O < 0.01	K_2O < 0.01	TiO_2 0.022	P_2O_5 0.02					
Trace	V	Cr	Co	Ni	Cu	Zn	Ga	Ge	As	Rb	Sr	Y	Zr			
	< 5	20	7	80	10	20	1	< 1	14	< 2	11	< 1	22			
	Nb	Mo	Ag	Sn	Sb	Cs	Ba	W	Tl	Pb	Bi	Th	U			
	< 1	27	< 0.5	1	3.7	< 0.5	39	< 1	0.8	12	< 0.4	0.2	0.4			

these pyrites, the oxidation rate was 0.28 ± 0.03 nm.day^{-1}. Iron sulfate (a whitish mineral) was macroscopically visible soon (~ 500 h, sulfate peak also observed by XPS) and continued to increase during the progress of the experiment (e.g., 5000 h, Fig. 3C). This was confirmed by XPS surface data with the proportion of sulfate increasing over sulfides (Fig. 5A). Few Fe-oxides (a blackish mineral, e.g., 10,000 h, Fig. 3C) were observed later, with traces already being visible after 2000 h of experiment. After 10,000 h, air-exposed pyrites (Fig. 3C) were macroscopically distinct from fresh ones (Fig. 1E).

In the drip exposure experiment (Fig. 3B), the oxidation depth over time was almost linear ($y = 0.487x$, $R^2 = 0.98$) over the whole exposure time (4500 h) with a slight decrease of the slope at later exposure time (> 3500 h). Oxidation depth was close to 1000 nm after the first 2,000 h and reached ~ 2000 nm at 4000 h of exposure. This results in an oxidation rate of 11.7 ± 1.8 nm day^{-1}. Very quickly, a heterogeneous layer of Fe-oxides with few discrete sulfates appeared macroscopically on the surface of the pyrite samples (Fig. 3C, ~ 2500 h). At 5,000 h, oxidation was well established and almost homogeneously covered the pyrite surface while sulfates were almost absent. These observations were confirmed by XPS indicating the presence of iron oxides and pyrite at 2298 h (Fig. 5B). The almost fully oxidized surface at 4085 h lacked a peak of Fe–S (pyrite) (Fig. 5B).

Discussion

Structure and chemistry of pyrite

Natural specimens of pyrite do not have ideal chemistry (FeS_2) and contain small quantities of minor and trace elements (Co, Ni, As, …), even if in most specimen/samples the ratio of molar proportions of Fe and S is close to 1:2 (Abraitis et al. 2004). For example, Doyle and Mirza (1996) determined the S/Fe ratio via electron probe microanalysis with values ranging from 1.983 to 2.015, which corresponds to less than 1% deviation from the ideal formula without considering the influence of trace elements. Oberthur et al. (1997) report average compositions of pyrite from the Great Dyke (Zimbabwe) as 45.44 wt.% Fe and 53.25 wt.% S (molar ratio S/Fe ~ 2.041) with Co and Ni as minor elements of less than 2 wt.%. However, such minor deviations from ideal stoichiometry could have important consequences regarding the electrical properties of the mineral (Abraitis et al. 2004). In pyrite, lattice substitutions can be either stoichiometric or non-stoichiometric. Stoichiometric substitutions mainly result from Co^{2+} and Ni^{2+} replacing Fe^{2+}, and Se or Te replacing S (Abraitis et al. 2004). The most common

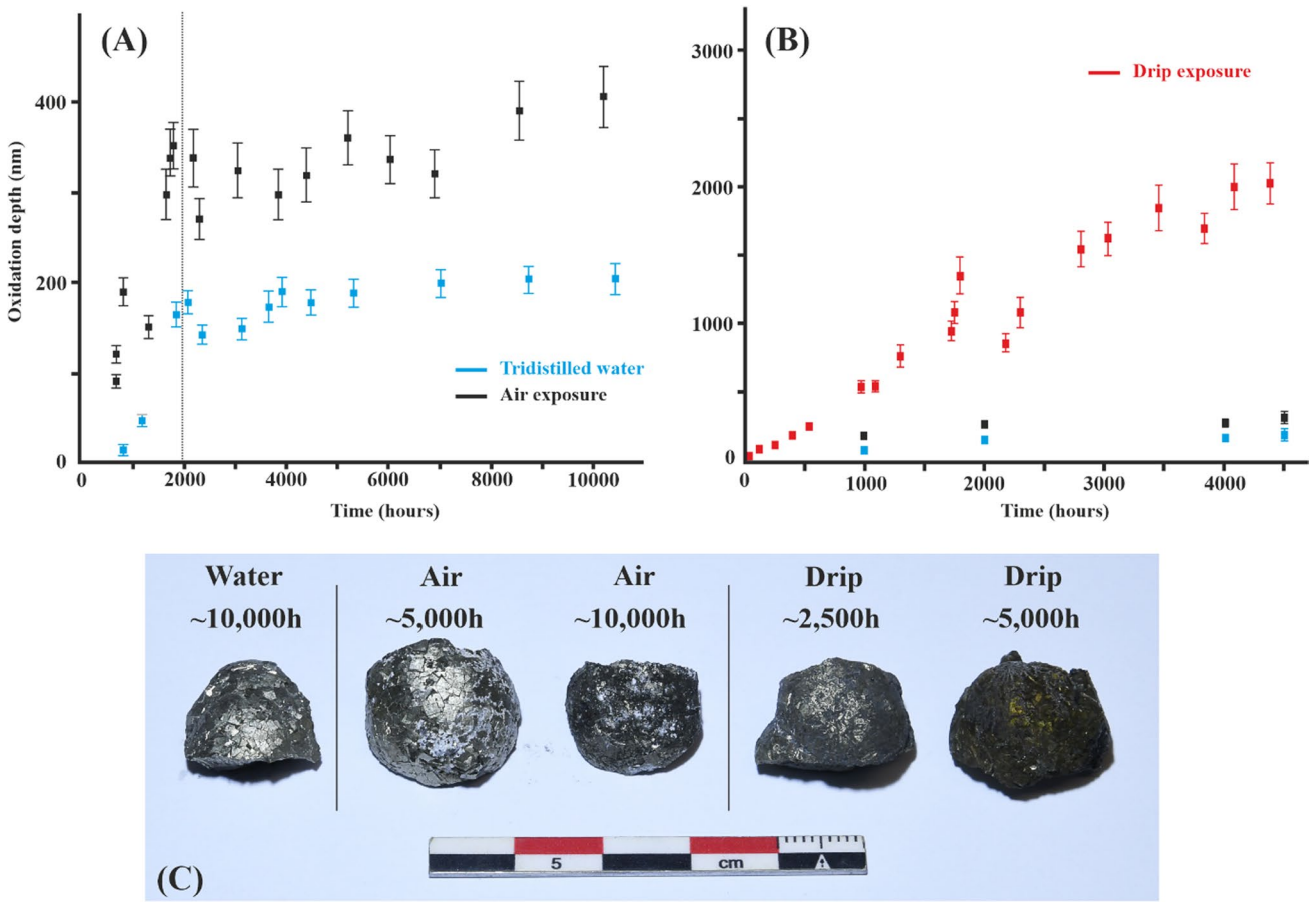

Fig. 3 Pyrite oxidation depth over time under air exposure, in tridistilled water (**A**, **B**), and under drip exposure (**B**). **C** Macroscopic evolution of pyrite over time in the different experiments

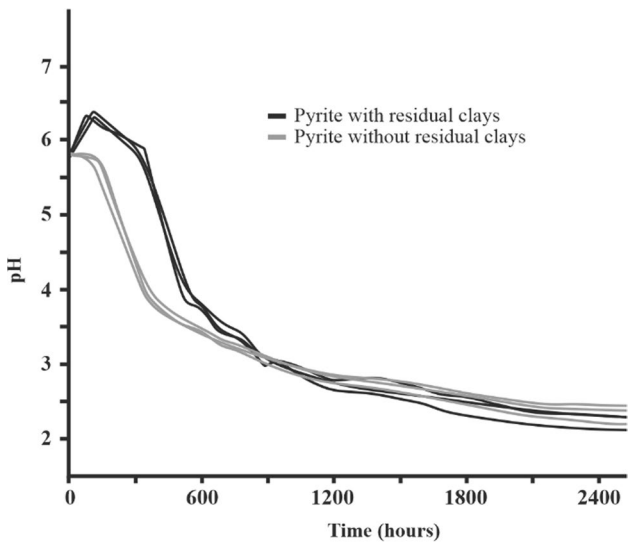

Fig. 4 Evolution of pH for pyrite in tridistilled water with and without residual clay

non-stoichiometric substitutions in pyrite include the incorporation of As by substituting Fleischer (1955) and Vaughan and Craig (1978) found the following maximum contents for minor elements in pyrite: As (5 wt.%), Pb (5,000), V (1,000), Sb (700), Ti (600), Sn (400), Tl (340), Se (300), Ag (200), Au (200), Ga (100), Bi (100), Ge (50), Mo (30), Cd (10), In (10) and Hg (0.4) (all concentrations given in wt.ppm except As). Several authors (Wells and Mullens 1973; Huston et al. 1995; Oberthur et al. 1997; Large et al. 2009; Sykora et al. 2018; Steadman et al. 2021) determined minor and trace elements in pyrite (Table 3).

Our studied pyrite samples show an S/Fe ratio of 2.018, which is very close to the ideal stoichiometry. The low percentage of SiO_2, Al_2O_3 and other oxides (Table 2) may be associated with very low clay contents in the microfractures/structures of the pyrite. Moreover, the main minor elements (Table 3) are present in very low concentrations, indicating a lack of inclusions of other sulfide minerals. Thus, the stability, and hence, oxidation rate of the pyrite samples studied here is only slightly or even unaffected by trace elements.

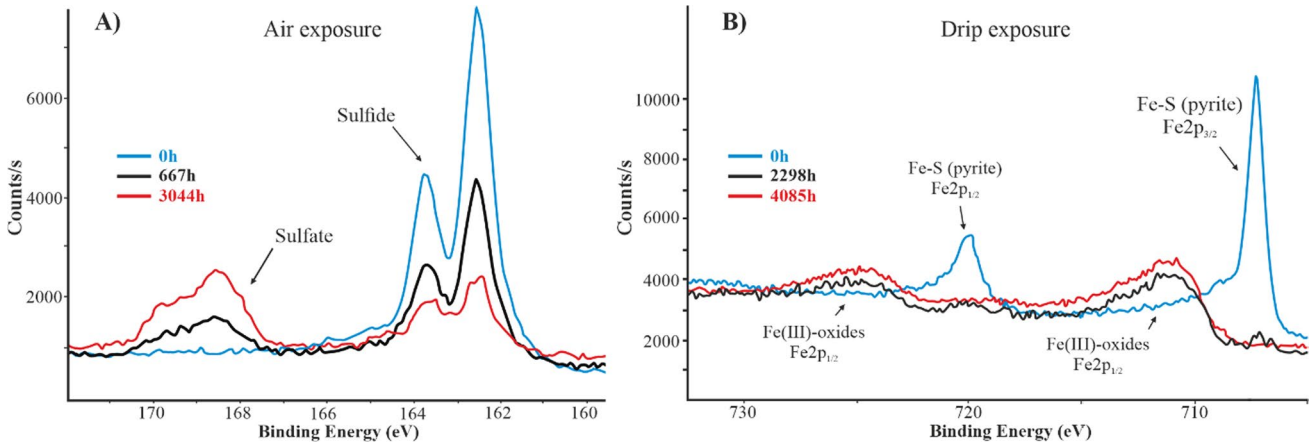

Fig. 5 **A** XPS spectrum of sulfates and sulfides on the surface of air exposed pyrite (at 667 h and 3044 h). **B** XPS spectrum of Fe (pyrite or/and oxides) on the surface of drip exposed pyrite (at 2298 h and 4085 h)

Table 3 Range or maximum values for main minor elements in pyrite (in wt.ppm or *wt.%)

	Co	Ni	Pb	Zn	Cu	As	Sb	Au
Steadman et al. (2021)	100–1*	10–0.5*	50	–	–	500–1*	–	50
Abraitis et al. (2004)	2.2*	0.2*	0.9*	0.9*	–	9.6*	0.6*	0.3*
Oberthur et al. (1997)	1.45*	0.2*	96	9	0.2*	6		
Huston et al. (1995)	590–2.16*	300–640	330–0.87*	580–0.94*	0.22*–4.52*	16–4.67*	25–0.73*	20–210
Wells and Mullens (1973)	–	–	–	–	–	0.79*–9.6*	0.12*–0.56*	0.15*–0.35*
Fleischer (1955), Vaughan and Craig (1978)	–	–	0.5*	–	–	5*	700	200
This study	**7**	**80**	*12*	**20**	**10**	**14**	**3.7**	–

Values are in wt.ppm except for values with * that are in wt.%

Pyrite oxidation rate: comparison and geological extrapolation

Pyrite oxidation rates have already been studied using modeling based on specific surface area. Several authors (e.g., McKibben and Barnes 1986; Pesic et al. 1989; Nicholson et al. 1990; Moses and Herman 1991; Williamson and Rimstidt 1994; Holmes and Crundwell 2000; Kameia and Ohmotob 2000; Jerz and Rimstidt 2004; Huminicki and Rimstidt 2009; Wang et al. 2019; Verron et al. 2019) defined laws for pyrite oxidation under different experimental setups (Table 4). Most of these models use the specific area ($m^2.g^{-1}$) of the pyrite and therefore the surface reaction rate ($mol.m^{-2}.s^{-1}$) calculated by dividing the amount of change in reactants or products by the total surface area of pyrite. These equations generally apply only under precise experimental conditions and are very difficult to use in geological applications that require extrapolation over millions of years.

Wang et al. (2019) propose a rate model that includes the rate of pyrite destruction and the rate of unreacted core shrinking. Their model assumes that a diffusion barrier around fresh pyrite forms as a thin layer predominantly by precipitation of oxides, which decreases the diffusion of oxygen to the pyrite surface over time. Some other authors (Garrels and Thompson 1960; Huminicki and Rimstidt 2009; Wang et al. 2022) also mention the presence of a thin layer of ferrous sulfate, iron oxides and sulfuric acid on the pyrite surface that delays oxygen transport. However, Manaka (2023) considers that the oxy-hydroxides layer do not passivate the oxidation of pyrite. In carbonated systems, the precipitation of gypsum or anhydrite (sulfates) with calcium and sulfuric acid could have two opposed effects: (i) the same barrier effect as mentioned above; (ii) the consumption of sulfates could favor pyrite oxidation (Verron et al. 2019) according to the Le Châtelier principle. Verron et al. (2019) mention that the addition of clay phases or other detrital silicates has no impact on pyrite oxidation rate.

Our study based on new XPS analyses provides pyrite oxidation rates that can be extrapolated (linear regression) considering that the barrier effect of sulfates (and oxides)

Table 4 Examples of laws for pyrite oxidation rates

References	Oxidation rate law	Unit	Comments
McKibben and Barnes (1986)	$r_{Py,O_2} = -10^{-9.77} M_{DO}^{0.5}$ $r_{Py,Fe^{3+}} = -10^{-9.74} M_{Fe^{3+}}^{0.5} M_{H^+}^{-0.5}$	mol cm^{-2} min^{-1}	pH 2–4, 20–40°C
Nicholson et al. (1990)	$r_{Py,O_2} = \alpha R^2 / \left(\frac{R(R-r)}{rD_s} + \frac{R^2}{r^2 k^e} \right)$		pH 6.7–7.5
Moses and Herman (1991)	$r_{Py,O_2} = 10^{-3.23} \left(\frac{A}{V} \right)$		pH 6–7
Williamson and Rimstidt (1994)	$r_{Py,O_2} = 10^{-8.19(\pm 0.1)} M_{DO}^{0.5(\pm 0.04)} M_{H^+}^{-0.11(\pm 0.01)}$ $r_{Py,Fe^{3+}} = 10^{-6.07(\pm 0.57)} M_{Fe^{3+}}^{0.93(\pm 0.07)} M_{Fe^{2+}}^{-0.4(\pm 0.06)}$	mol m^{-2} s^{-1}	pH 2–10
Holmes and Crundwell (2000)	$r_{Py,O_2} = k[H^+]^{-0.18}[O_2]^{0.5}$		pH 1.5–3.5
Kameia and Ohmotob (2000)	$r_{Py,O_2} = 10^{-5.3 \pm 0.5} M_{DO}$	mol m^{-2} s^{-1}	pH 5.7 ± 0.3
Jerz and Rimstidt (2004)	$r_{Py,O_2} = 10^{-6.6} P^{0.5} t^{-0.5}$	mol m^{-2} s^{-1}	Neutral pH, 25°C
Verron et al. (2019)	$r_{Py} = 10^{-4.8} {P_{O_2}}^{0.5} t^{-0.5}$ $r_{Py+Ca} = 10^{-5.1} {P_{O_2}}^{0.5} t^{-0.5}$	mol m^{-2} s^{-1}	100°C

on the surface is constant and therefore, oxidation is also constant over time. This regression/assumption leads to an average oxidation rate of about 0.10 ± 0.02 m.Ma^{-1} under air exposure. The same approach applied for the data from the drip exposure experiment results in an oxidation rate of 4.3 ± 0.6 m.Ma^{-1}. However, the assumption is only valid with regards to the oxides' barrier since sulfates are almost entirely leached. These two oxidation rates are different. In the case of air exposure, only the ambient humidity plays a role in the weathering of pyrite. Furthermore, the mineral phases that form on the surface (mainly sulfates) are not leached which probably increases the sulfate barrier effect mentioned by (Butler and Rickard 2000) compared to the drip exposure experiment. Underwater pyrite is almost unaffected by oxidation with values remaining below 1 cm. Ma^{-1}.

Although the presence of clays slightly buffered pH values in the experiment with tridistilled water during the oxidation of pyrite (Fig. 4), the effect was very limited and vanished over time. Nevertheless, pyrite from the Danube–Bouchon quarry is embedded in clay (Hautrage Clay Formation), which preserved them from the oxidizing conditions on the surface. Furthermore, it has already been demonstrated that chlorite (Brown 1967) or even carbonates

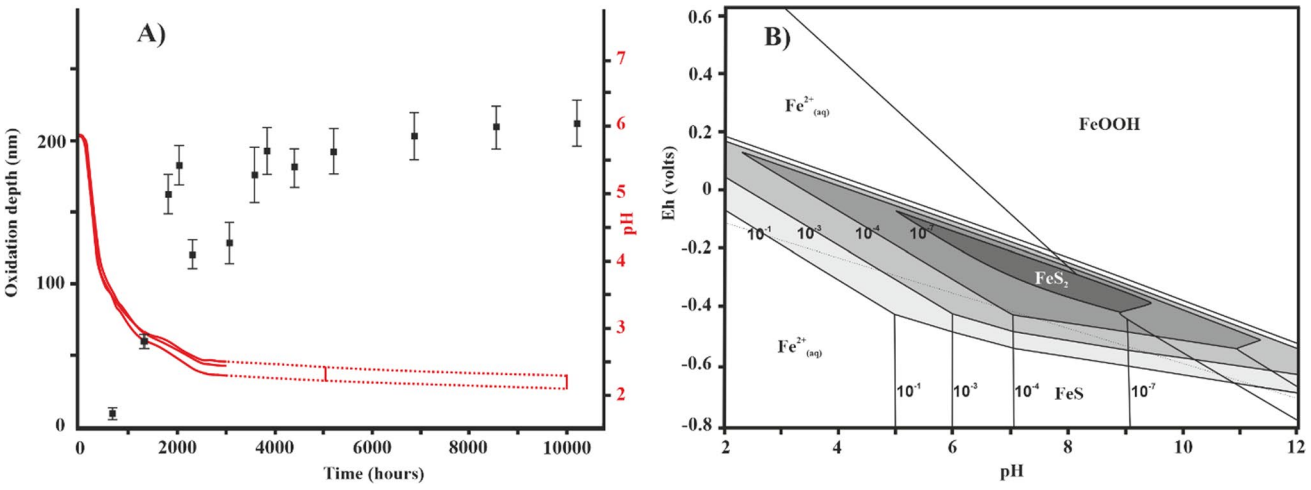

Fig. 6 **A** Oxidation depth vs. pH evolution over time for pyrite in tridistilled water. **B** Eh–pH stability field diagram for the system Fe–S–H_2O at 25 °C. Increasing total Fe and S concentrations (10^{-7}–10^{-1} m) result in an increase in the extent of the FeS_2 stability field (grey) (Butler and Rickard 2000)

(Descostes et al. 2002) present in the solution/rock can neutralize acidic fluids, which will play a significant part in the regulation of the pH and the subsequent oxidation process. Thus, the evolution of the pH will have an impact on the oxidation of pyrite (McKibben and Barnes 1986; Williamson and Rimstidt 1994; Jerz and Rimstidt 2004; Wang et al. 2019; Verron et al. 2019).

According to our data on the evolution of pH and oxidation depth for pyrite in water (Fig. 6A), the first rapid oxidation induces a simultaneous drop in pH and is mainly due to the oxygen dissolved in the water, which is consumed to oxidize the pyrite. Once this amount of dissolved oxygen has been depleted, only trace amounts of oxygen are introduced into the system via the exchange between the atmosphere and the closed plastic pot containing tridistilled water and pyrite. The diffusion coefficient of oxygen in water is also relatively low. As a result, the evolution of pyrite oxidation and pH is constant but much slower (Fig. 6A), which is confirmed by a stability field diagram (Fig. 6B) that assumes that pyrite can be stable at low pH with an Eh close to zero (Butler and Rickard 2000).

Consequences for weathering profiles

Our experimental data can be related to different zones of weathering profiles (Fig. 7). Our drip exposure experiment can be associated with the vadose zone, where rainfall and runoff oxidize and leach pyrite in laterite and saprolite parts of the weathering profile. Thus, the average oxidation rate should range between the two values we determined via drip (4.3 ± 0.6 m.Ma^{-1}) and air exposure (0.10 ± 0.02 m.Ma^{-1}), since most regions of the world experience both drier and wetter seasons. Dry periods promote the formation of sulfates while wet periods would favor leaching and the development of oxidized levels. Because sulfides are stable below the water table level under reducing conditions, our observations on pyrite in water can also be extrapolated to weathering profiles, referring to the cementation zone (secondary sulfides) (Guilbert and Park 1986; Brookins 1988; Robb 2005).

Regarding pyrite oxidation rates in geological conditions, our results are similar to those of Lapakko and Antonson (2006) (Table 5). The latter authors show that pyrite oxidation rates, normalized for exposed surface area, range from 4×10^{-10} to 18×10^{-10} mol m^{-2} s^{-1}. If we convert their data, considering the molecular weight of pyrite (119.975 g mol^{-1}) and its density (5 g.cm^{-3}), we obtain an oxidation rate of 1.36 m.Ma^{-1}. This oxidation rate lies between the two values (air and drip exposure) observed experimentally in this study.

Experimentally obtained weathering rates are probably lower than actual weathering rates in the geological field. As White and Brantley (2003) have shown with a study on silicate minerals, the weathering rate depends on (i) intrinsic characteristics of the mineral/fluids, and (ii) extrinsic characteristics related to the weathering environment. Intrinsic

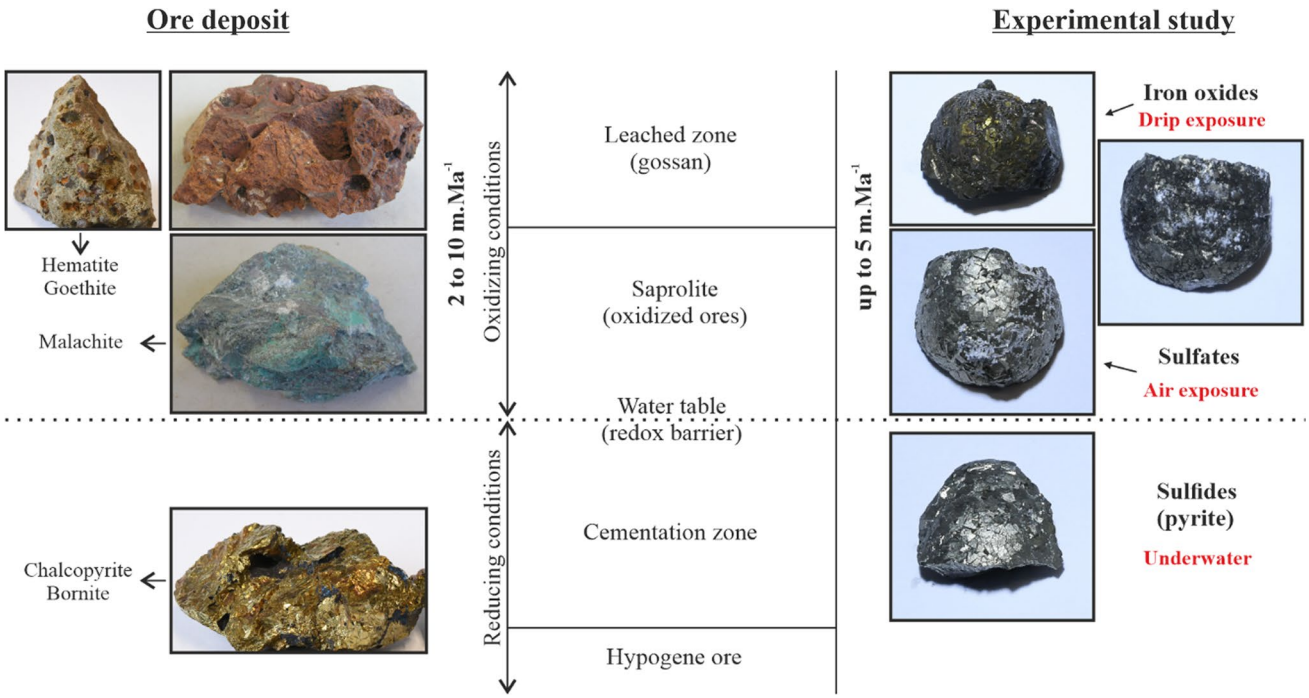

Fig. 7 Comparison between our experimental study on pyrite oxidation and geological weathering profiles

Table 5 Oxidation/weathering rate for minerals, rocks and profiles, based on various geological methods

	References	Oxidation/Weathering rate	Comments
Mineral/Rock experiment	This study	4.3 m Ma^{-1}	Pyrite
	Lapakko and Antonson (2006)	4×10^{-10} to 18×10^{-10} mol m^{-2} s^{-1} 1.36 m Ma^{-1}	Pyrite
	Sun et al. (2019)	$R=7.0$ t km^{-2} y^{-1} 2.59 m Ma^{-1}	Silicate weathering rate—Granite
Isotopic datation on profile	Dequincey et al. (1999)	6 to 8 m Ma^{-1}	Goyoum Laterite (Cameroun) – $^{234}U/^{238}U$ dating Kaolinite and Fe-(oxi)hydroxides Humid tropical climate
	de Oliveira Carmo and Vasconcelos (2006)	8.9 ± 1.1 m Ma^{-1} 24.9 ± 3.1 t/km^2/year	Weathering front propagation—$^{40}Ar/^{39}Ar$ Saprolitization rate (Cachoeira Mine, Brazil)
	Vasconcelos and Conroy (2003)	3.8 m Ma^{-1}	Weathering rate—$^{40}Ar/^{39}Ar$ Dugald River area (Australia)
	Braun et al. (2012)	Min 2 to 10 m Ma^{-1}	Nsimi (South Cameroun) Saprolite rate production (Eocene)
	Braun et al. (2012)	~2 m Ma^{-1}	Mule Hole SEW (South India)
	De Putter et al. (2015)	$\geq$7.7 m Ma^{-1} ($\geq$100 m in 13 Ma)	Kisenge Mn deposit (Katanga, DRC)

effects include increased physical surface area due to surface roughness, concurrent decrease in reactive surface area due to reduced compositional and structural heterogeneities, and physical occlusion by secondary minerals (see discussion above). Extrinsic factors might have a significant effect but are more difficult to reproduce in the laboratory. In contrast to natural/geological weathering, which involves much lower fluid/mineral interactions over much longer time periods, experimental rates are measured with high fluid/mineral ratios reacting over short periods of time. Sun et al. (2019) simulated an average silicate (granite) weathering rate of 7.0 t km^{-2} y^{-1}, which corresponds to 2.6 m Ma^{-1} (calculated with a granite density of 2.7). Other studies estimated weathering rates using different dating methods. Dequincey et al. (1999) estimated the weathering rate of Goyoum laterite (Cameroum) via radioactive disequilibria ($^{234}U/^{237}U$), based on the hypothesis that the measured disequilibria represent geochemical fractionations that would be characteristic for the formation and evolution of laterite profiles. The resulting weathering rate of 6–8 m Ma^{-1} is higher but still comparable to our experimental data considering the humid tropical climate of the area in Cameroun (promoting the leaching of sulfates) in addition to the fact that experimental data slightly underestimated geological values. de Oliveira Carmo and Vasconcelos (2006) studied grains of cryptomelane in the Cachoeira Mine weathering profile, Minas Gerais (SE Brazil), and estimated the weathering front propagation rate, measured by $^{40}Ar/^{39}Ar$ ages, to be 8.9 ± 1.1 m Ma^{-1}, which corresponds to a saprolitization rate of 24.9 ± 3.1 tkm^{-2} y^{-1}. Vasconcelos and Conroy (2003) conducted a similar study with grains of supergene jarosite, alunite, and cryptomelane from weathering profiles in the

Table 6 Main factors influencing oxidation/weathering rates in geological profiles. Effect + will increase the rate of weathering profile; effect - will decrease the rate of weathering profile

References	Parameters	Effects
Fricke and O'Neil (1999), Boni and Large (2003)	Climate change over time (rainfall, temperature, CO_2 in atmosphere, …)	±
White and Brantley (2003), Choulet et al. (2014), Boni and Mondillo (2015), Verhaert et al. (2017), Sillitoe (2019)	Oxidizing environment	+
Boni and Mondillo (2015), Ciantia and Castellanza (2016)	Nature of the host rock for neutralization processes	±
Borg (2009), Choulet et al. (2014), Boni and Mondillo (2015)	Faulting and fractures/porosity of host rocks	+
White and Brantley (2003), Jerz and Rimstidt (2004), Wang et al. (2019)	Secondary mineralization precipitation/occlusion	–
Wilson (2004)	Nature of primary mineralization	±
De Putter et al. (2010), Korehi et al. (2013), Vera et al. (2013)	Bacteria acting as catalysts	+

Dugald River area (Australia) using $^{40}Ar/^{39}Ar$ dating and estimated a weathering rate of 3.8 m.Ma^{-1}. These values correspond to our data, as other weathering rates (Table 5).

All of these weathering rates are therefore close to the experimental ones. However, deposits in natural systems do not predominantly consist of pure pyrite (or more generally sulfides). Mineral inclusions in pyrite such as galena or sphalerite (up to 0.9 wt.% of Pb and Zn) can occur and are generally associated with arsenian pyrite, which is strongly correlated with high contents of Au (Table 3) (Large et al. 2009). These sulfides are embedded in a host rock with variable chemical–mineralogical–petrographical compositions, porosities, fractures, and catalysts such as bacteria. These geological parameters (Table 6), as well as climate change over time (Boni and Large 2003), will influence the weathering rate. The role of bacteria (thiosulfates) is not observed in our experiments but could play a role in the pyrite oxidation process in natural systems.

Conclusion

This study provides new experimental data on the oxidation rate of pyrite, using X-ray Photoelectron Spectroscopy (XPS). This technique allows to measure the thickness of the oxidation layer under air, water or drip exposure by performing elemental (O, Fe, S) depth profiles. In addition, the technique detects the presence of surface minerals such as sulfate, sulfide or iron oxide. Pyrite in tridistilled water showed only a very limited rate of oxidation, as well as pyrite exposed to air that oxidized only slightly, showing varying degrees of sulfate precipitation at the surface. Pyrite under drip exposure exhibited the highest oxidation rate at 0.28 ± 0.03 nm day^{-1}. By extrapolation to geological weathering profiles, this oxidation rate could reach up to 4.3 ± 0.6 m Ma^{-1}, which is consistent to numerous studies based on isotopic dating. Nevertheless, various parameters may explain variations between experimental and geological rates of weathering profiles, such as: (i) the nature of the host rock (protore) including the primary mineralogy (a deposit is rarely composed solely of sulfides), ii) its porosity/permeability and fractures, (iii) the presence of an oxidizing or non-oxidizing environment, (iv) climate change over time, (v) the action of bacteria as catalysts.

Supplementary Information The online version contains supplementary material available at https://doi.org/10.1007/s12665-023-11325-z.

Author contributions All authors contributed to the study conception and design. Samples were collected and prepared by POOT Julien, LEPÊCHEUR Guillaume and ROCHEZ Gaëtan. XPS analysis and data processing were carried out by POOT Julien, FELTEN Alexandre, COLAUX Julien and GOUTTEBARON Rachel. All authors contributed to and approved the final manuscript.

Funding This study was conducted without external funding.

Data availability Data used in this paper are available under request to the corresponding author.

Declarations

Conflict of interest The authors declare no conflict of interest.

References

Abraitis PK, Pattrick RAD, Vaughan DJ (2004) Variations in the compositional, textural and electrical properties of natural pyrite: a review. Int J Miner Process 74:41–59. https://doi.org/10.1016/J.MINPRO.2003.09.002

Barral A, Gomez B, Zorrilla JM et al (2016) Local-scale analysis of plant community from the Early Cretaceous riparian ecosystem of Hautrage, Belgium. Palaeogeogr Palaeoclimatol Palaeoecol 443:107–122. https://doi.org/10.1016/J.PALAEO.2015.11.026

Barral A, Gomez B, Zorrilla JM et al (2017) Analysing the representativeness of local-scale palaeodiversity measurements: a case from the Lower Cretaceous plant assemblage of Hautrage (Mons Basin, Belgium). Lethaia 50:244–257. https://doi.org/10.1111/LET.12194

Boni M, Large D (2003) Nonsulfide zinc mineralization in Europe: an overview. Econ Geol 98:715–729. https://doi.org/10.2113/98.4.7

Boni M, Mondillo N (2015) The "Calamines" and the "Others": the great family of supergene nonsulfide zinc ores. Ore Geol Rev 67:208–233. https://doi.org/10.1016/j.oregeorev.2014.10.025

Borg G (2009) The Influence of Fault Structures on the Genesis of Supergene Zinc Deposits. In: Supergene environments, processes, and products, society of economic geologists special publication 14:121–132. https://doi.org/10.5382/SP.14

Braun JJ, Marechal JC, Riotte J et al (2012) Elemental weathering fluxes and saprolite production rate in a Central African lateritic terrain (Nsimi, South Cameroon). Geochim Cosmochim Acta 99:243–270. https://doi.org/10.1016/J.GCA.2012.09.024

Brookins DG (1988) Eh-pH Diagrams for Geochemistry. Springer-Verlag, Berlin, p 176. https://doi.org/10.1016/0016-7037(89)90020-3

Brown EH (1967) The greenschist facies in part of eastern Otago, New Zealand. Contrib Miner Pet 14:259–292. https://doi.org/10.1007/BF00373808

Buckley AN, Woods R (1987) The surface oxidation of pyrite. Appl Surf Sci 27:437–452. https://doi.org/10.1016/0169-4332(87)90153-X

Butler IB, Rickard D (2000) Framboidal pyrite formation via the oxidation of iron (II) monosulfide by hydrogen sulphide. Geochim Cosmochim Acta 64:2665–2672. https://doi.org/10.1016/S0016-7037(00)00387-2

Choulet F, Charles N, Barbanson L et al (2014) Non-sulfide zinc deposits of the Moroccan High Atlas: Multi-scale characterization and origin. Ore Geol Rev 56:115–140. https://doi.org/10.1016/j.oregeorev.2013.08.015

Ciantia MO, Castellanza R (2016) Modelling weathering effects on the mechanical behaviour of rocks. Europ J of Envi and Civil Eng 20:1054–1082. https://doi.org/10.1080/19648189.2015.1030086

de Oliveira CI, Vasconcelos PM (2006) ^{40}Ar / ^{39}Ar geochronology constraints on Late Miocene weathering rates in Minas Gerais, Brazil. Earth Planet Sci Lett 241:80–94. https://doi.org/10.1016/J.EPSL.2005.09.056

De Putter T, Mees F, Decrée S, Dewaele S (2010) Malachite, an indicator of major Pliocene Cu remobilization in a karstic environment (Katanga, Democratic Republic of Congo). Ore Geol Rev 38:90–100. https://doi.org/10.1016/J.OREGEOREV.2010.07.001

De Putter T, Ruffet G, Yans J, Mees F (2015) The age of supergene manganese deposits in Katanga and its implications for the Neogene evolution of the African Great Lakes Region. Ore Geol Rev 71:350–362. https://doi.org/10.1016/J.OREGEOREV.2015.06.015

Dequincey O, Chabaux F, Clauer N et al (1999) Dating of weathering profiles by radioactive disequilibria: Contribution of the study of authigenic mineral fractions. Comptes Rendus De L'academie De Sciences - Serie IIa: Sciences De La Terre Et Des Planetes 328:679–685. https://doi.org/10.1016/S1251-8050(99)80177-3

Descostes M, Beaucaire C, Mercier F et al (2002) Effect of carbonate ions on pyrite (FeS_2) dissolution. Bull Soc Geol Fr 173:265–270. https://doi.org/10.2113/173.3.265

Doyle FM, Mirza AH (1996) Electrochemical oxidation of pyrite samples with known composition and electrical properties. Electrochem Proc 96:203–214

Dupuis C, Vandycke S (1989) Tectonics and deep karstification: a model of original subsidence for the Mons Basin. Annales-Societe Geologique De Belgique 112:479–487

Eggleston CM, Ehrhardt JJ, Stumm W (1996) Surface structural controls on pyrite oxidation kinetics: an XPS-UPS, STM, and modeling study. Am Miner 81:1036–1056. https://doi.org/10.2138/am-1996-9-1002

Ferris FG, Tazaki K, Fyfe WS (1989) Iron oxides in acid mine drainage environments and their association with bacteria. Chem Geol 74:321–330. https://doi.org/10.1016/0009-2541(89)90041-7

Fleischer M (1955) Minor elements in some sulfide minerals. In: Econ Geol Fiftieth Anniversary Vol: 1905–1955. https://doi.org/10.5382/AV50.24.

Fricke HC, O'Neil JR (1999) The correlation between $^{18}O/^{16}O$ ratios of meteoric water and surface temperature: Its use in investigating terrestrial climate change over geologic time. Earth Planet Sci Lett 170:181–196. https://doi.org/10.1016/S0012-821X(99)00105-3

Garrels RM, Thompson ME (1960) Oxidation of pyrite by iron sulfate solutions. Am J Sci 258:57–67

Guilbert JM, Park CF (1986) The Geology of Ore Deposits. W. H. Freeman and Company, New York, p 985

Harvey DT, Linton RW (1981) Chemical characterization of hydrous ferric oxides by x-ray photoelectron spectroscopy. Anal Chem 53:1684–1688. https://doi.org/10.1021/ac00234a030

Holmes PR, Crundwell FK (2000) The kinetics of the oxidation of pyrite by ferric ions and dissolved oxygen: An electrochemical study. Geochim Cosmochim Acta 64:263–274. https://doi.org/10.1016/S0016-7037(99)00296-3

Huminicki DMC, Rimstidt JD (2009) Iron oxyhydroxide coating of pyrite for acid mine drainage control. Appl Geochem 24:1626–1634. https://doi.org/10.1016/J.APGEOCHEM.2009.04.032

Huston DL, Sie SH, Suter GF et al (1995) Trace elements in sulfide minerals from eastern Australian volcanic-hosted massive sulfide deposits: part I. Proton microprobe analyses of pyrite, chalcopyrite, and sphalerite, and part II. Selenium levels in pyrite: comparison with δ34S values and impli. Econ Geol 90(5):1167–1196. https://doi.org/10.2113/gsecongeo.90.5.1167

Hyland MM, Bancroft GM (1990) Palladium sorption and reduction on sulphide mineral surfaces: an XPS and AES study. Geochim Cosmochim Acta 54:117–130. https://doi.org/10.1016/0016-7037(90)90200-5

Jerz JK, Rimstidt JD (2004) Pyrite oxidation in moist air. Geochim Cosmochim Acta 68:701–714. https://doi.org/10.1016/S0016-7037(03)00499-X

Jones CF, LeCount S, Smart RSC, White TJ (1992) Compositional and structural alteration of pyrrhotite surfaces in solution: XPS and XRD studies. Appl Surf Sci 55:65–85. https://doi.org/10.1016/0169-4332(92)90382-8

Kameia G, Ohmotob H (2000) The kinetics of reactions between pyrite and O_2-bearing water revealed from in situ monitoring of DO, Eh and pH in a closed system. Geochim Cosmochim Acta 64:2585–2601. https://doi.org/10.1016/S0016-7037(00)00384-7

Karthe S, Szargan R, Suoninen E (1993) Oxidation of pyrite surfaces: a photoelectron spectroscopic study. Appl Surf Sci 72:157–170. https://doi.org/10.1016/0169-4332(93)90007-X

Kefeni KK, Msagati TAM, Mamba BB (2017) Acid mine drainage: prevention, treatment options, and resource recovery: a review. J Clean Prod 151:475–493. https://doi.org/10.1016/J.JCLEPRO.2017.03.082

Korehi H, Blöthe M, Sitnikova MA et al (2013) Metal mobilization by iron- and sulfur-oxidizing bacteria in a multiple extreme mine tailings in the Atacama Desert, Chile. Environ Sci Technol 47:2189–2196. https://doi.org/10.1021/ES304056N/SUPPL_FILE/ES304056N_SI_001.PDF

Lapakko KA, Antonson DA (2006) Pyrite oxidation rates from humidity cell testing greenstone rock. J Am Soc Min Reclam 2:1007–1025. https://doi.org/10.21000/JASMR06021007

Large RR, Danyushevsky L, Hollit C et al (2009) Gold and trace element zonation in pyrite using a laser imaging technique: implications for the timing of gold in orogenic and carlin-style sediment-hosted deposits. Econ Geol 104:635–668. https://doi.org/10.2113/gsecongeo.104.5.635

Manaka M (2023) Extent of pyrite oxidation by dissolved oxygen in alkaline solutions including purified sodium bentonite. Appl Geoch 148:105548. https://doi.org/10.1016/j.apgeochem.2022.105548

Marlière R (1954) Le Crétacé. In: Prodrome d'une description géologique de la Belgique. Annales de la Société géologique de Belgique, Publications spéciales 417–444

McKibben MA, Barnes HL (1986) Oxidation of pyrite in low temperature acidic solutions: Rate laws and surface textures. Geochim Cosmochim Acta 50:1509–1520. https://doi.org/10.1016/0016-7037(86)90325-X

Melashvili M, Fleming C, Dymov I, Matthews D, Dreisinger D (2015) Equation for thiosulphate yield during pyrite oxidation. Miner Eng 74:105–111. https://doi.org/10.1016/j.mineng.2015.02.004

Mills P, Sullivan JL (1983) A study of the core level electrons in iron and its three oxides by means of X-ray photoelectron spectroscopy. J Phys D Appl Phys 16:723–732. https://doi.org/10.1088/0022-3727/16/5/005

Moses CO, Herman JS (1991) Pyrite oxidation at circumneutral pH. Geochim Cosmochim Acta 55:471–482. https://doi.org/10.1016/0016-7037(91)90005-P

Neculita C-M, Zagury GJ, Bussière B (2007) Passive treatment of acid mine drainage in bioreactors using sulfate-reducing bacteria: critical review and research needs. J Environ Qual 36:1–16. https://doi.org/10.2134/jeq2006.0066

Nicholson VR, Gillham RW, Reardon EJ (1990) Pyrite oxidation in carbonate-buffered solution: 2. Rate control by oxide coatings. Geochim Cosmochim Acta 54:395–402. https://doi.org/10.1016/0016-7037(90)90328-I

Nordstrom DK (1982) The effect of sulfate on aluminum concentrations in natural waters: some stability relations in the system Al_2O_3-SO_3-H_2O at 298 K. Geochim Cosmochim Acta 46(4):681–692. https://doi.org/10.1016/0016-7037(82)90168-5

Nyström E, Thomas H, Wanhainem C, Alakangas L (2021) Occurrence and release of trace elements in pyrite-rich waste rock. Minerals 11:495. https://doi.org/10.3390/min11050495

Oberthur T, Cabri L, Weisner T et al (1997) Pt, Pd and other trace elements in sulfides of the main sulfide zone, Great Dyke, Zimbabwe: a reconnaissance study. Can Mineral 35:597–609

Park I, Tabelin CB, Jeon S et al (2019) A review of recent strategies for acid mine drainage prevention and mine tailings recycling. Chemosphere 219:588–606. https://doi.org/10.1016/J.CHEMOSPHERE.2018.11.053

Pesic B, Oliver DJ, Wichlacz P (1989) An electrochemical method of measuring the oxidation rate of ferrous to ferric iron with oxygen in the presence of *Thiobacillus ferrooxidans*. Biotechnol Bioeng 33:428–439. https://doi.org/10.1002/BIT.260330408

Pratt AR, Muir IJ, Nesbitt HW (1994) X-ray photoelectron and Auger electron spectroscopic studies of pyrrhotite and mechanism of air oxidation. Geochim Cosmochim Acta 58:827–841. https://doi.org/10.1016/0016-7037(94)90508-8

Robb LJ (2005) Introduction to ore-forming processes. Blackwell Science Ltd, Oxford

Scheidegger A, Borkovec M, Sticher H (1993) Coating of silica sand with goethite: preparation and analytical identification. Geoderma 58:43–65. https://doi.org/10.1016/0016-7061(93)90084-X

Schnyder J, Dejax J, Keppens E et al (2009) An Early Cretaceous lacustrine record: organic matter and organic carbon isotopes at Bernissart (Mons Basin, Belgium). Palaeogeogr Palaeoclimatol Palaeoecol 281:79–91. https://doi.org/10.1016/J.PALAEO.2009.07.014

Sillitoe RH (2019) Supergene oxidation of epithermal gold-silver mineralization in the Deseado massif, Patagonia, Argentina: response to subduction of the Chile Ridge. Miner Depos 54:381–394. https://doi.org/10.1007/s00126-018-0814-4

Spagna P, Vandycke S, Dupuis C, Johan Y (2011) La Formation des Argiles d'Hautrage de la carrière Danube-Bouchon (Saint-Ghislain, Belgique): un enregistrement de la naissance et des premiers mouvements du Bassin de Mons au Crétacé Inférieur. Bulletin D'information Des Géologues Du Bassin De Paris 48:14–21

Spagna P, Yans J, Schnyder J, Dupuis C (2012) The paleoenvironment of the Bernissart Iguanodons: sedimentological analysis of the Lower Cretaceous Wealden facies in the Bernissart area (Belgium). In: Bernissart Dinosaurs and Early Cretaceous Terrestrial Ecosystems, Godefroit. Indiana University Press (USA), Indiana, p 648. http://www.jstor.org/stable/j.ctt16gzfhx. Accessed Feb 2023

Steadman JA, Large RR, Olin PH et al (2021) Pyrite trace element behavior in magmatic-hydrothermal environments: An LA-ICPMS imaging study. Ore Geol Rev 128:103678. https://doi.org/10.1016/j.oregeorev.2020.103878

Sun M, Wu W, Ji X et al (2019) Silicate weathering rate and its controlling factors: a study from small granitic watersheds in the Jiuhua Mountains. Chem Geol 504:253–266. https://doi.org/10.1016/J.CHEMGEO.2018.11.019

Sykora S, Cooke DR, Meffre S et al (2018) Evolution of pyrite trace element compositions from porphyry-style and epithermal conditions at the Lihir gold deposit: Implications for ore genesis and mineral processing. Econ Geol 113:193–208. https://doi.org/10.5382/econgeo.2018.4548

Van der Heide H, Hemmel R, van Bruggen CF, Haas C (1980) X-ray photoelectron spectra of 3d transition metal pyrites. J Solid State Chem 33:17–25. https://doi.org/10.1016/0022-4596(80)90543-5

Vandycke S, Bergerat F, Dupuis C (1991) Meso-cenozoic faulting and inferred palaeostresses in the Mons Basin, Belgium. Tectonophysics 192:261–271. https://doi.org/10.1016/0040-1951(91)90103-Y

Vasconcelos PM, Conroy M (2003) Geochronology of weathering and landscape evolution, Dugald River valley, NW Queensland, Australia. Geochim Cosmochim Acta 67:2913–2930. https://doi.org/10.1016/S0016-7037(02)01372-8

Vaughan D, Craig J (1978) Mineral chemistry of metal sulfides. Mineral Mag 43:186–187. https://doi.org/10.1180/minmag.1979.043.325.27

Vera M, Schippers A, Sand W (2013) Progress in bioleaching: fundamentals and mechanisms of bacterial metal sulfide oxidation—part A. Appl Microbiol Biotech 97:7529–7541. https://doi.org/10.1007/S00253-013-4954-2

Verhaert M, Bernard A, Dekoninck A et al (2017) Mineralogical and geochemical characterization of supergene Cu-Pb-Zn-V ores in the oriental High Atlas, Morocco. Miner Depos 52:1049–1068. https://doi.org/10.1007/s00126-017-0753-5

Verron H, Sterpenich J, Bonnet J et al (2019) Experimental study of pyrite oxidation at 100 °c: implications for deep geological rad-waste repository in claystone. Minerals 9:427. https://doi.org/10.3390/min9070427

Wang H, Dowd PA, Xu C (2019) A reaction rate model for pyrite oxidation considering the influence of water content and temperature. Miner Eng 134:345–355. https://doi.org/10.1016/j.mineng.2019.02.002

Wang Y, Liu X, Li Q (2022) Pyrite Oxidation under a Carbonate Buffer and Its Environmental Implications: a Case Study from the Shangmanggang Gold Deposit, SW China. Geochemistry Explor Environ Anal 22(4):10. https://doi.org/10.1144/geochem2022-021

Wanger CD, Riggs W, Davis LE et al (1979) Handbook of X-ray photoelectron spectroscopy. Wiley, p 190

Wells JD, Mullens TE (1973) Gold-bearing arsenian pyrite determined by microprobe analysis, Cortez and Carlin Gold Mines, Nevada. Econ Geol 68:187–201. https://doi.org/10.2113/gsecongeo.68.2.187

White AF, Brantley SL (2003) The effect of time on the weathering of silicate minerals: why do weathering rates differ in the laboratory and field? Chem Geol 202:479–506. https://doi.org/10.1016/j.chemgeo.2003.03.001

Williamson MA, Rimstidt JD (1994) The kinetics and electrochemical rate-determining step of aqueous pyrite oxidation. Geochim Cosmochim Acta 58:5443–5454. https://doi.org/10.1016/0016-7037(94)90241-0

Wilson MJ (2004) Weathering of the primary rock-forming minerals: processes, products and rates. Clay Miner 39:233–266. https://doi.org/10.1180/0009855043930133

Yans J (2007) Lithostratigraphie, minéralogie et diagenèse des sédiments à faciès wealdien du Bassin de Mons (Belgique). Académie royale de Belgique, Bruxelles, p 179 (**ISBN 978-2-8031-0237-2**)

Yans J, Dejax J, Pons D et al (2005) Implications paléontologiques et géodynamiques de la datation palynologique des sédiments à faciès wealdien de Bernissart (bassin de Mons, Belgique). C R Palevol 4:135–150. https://doi.org/10.1016/J.CRPV.2004.12.003

Yans J, Gerards T, Gerrienne P et al (2010) Carbon-isotope analysis of fossil wood and dispersed organic matter from the terrestrial Wealden facies of Hautrage (Mons Basin, Belgium). Palaeogeogr Palaeoclimatol Palaeoecol 291:85–105. https://doi.org/10.1016/J.PALAEO.2010.01.014